How Does Thermal Pressurization of Pore Fluids Affect 3D Strike-Slip Earthquake Dynamics and Ground Motions?

Jagdish Chandra Vyas*[1], Alice-Agnes Gabriel[2,3], Thomas Ulrich[3], Paul Martin Mai[1], and Jean-Paul Ampuero[4]

ABSTRACT

Frictional heating during earthquake rupture raises the fault-zone fluid pressure, which affects dynamic rupture and seismic radiation. Here, we investigate two key parameters governing thermal pressurization of pore fluids – hydraulic diffusivity and shear-zone half-width – and their effects on earthquake rupture dynamics, kinematic source properties, and ground motions. We conduct 3D strike-slip dynamic rupture simulations assuming a rate-and-state dependent friction law with strong velocity weakening coupled to thermal-pressurization of pore fluids. Dynamic rupture evolution and ground shaking are densely evaluated across the fault and Earth's surface to analyze the variations of rupture parameters (slip, peak slip rate, rupture speed, and rise time), correlations among rupture parameters, and variability of peak ground velocity. Our simulations reveal how variations in thermal-pressurization affect earthquake rupture properties. We find that the mean slip and rise time decrease with increasing hydraulic diffusivity, whereas mean rupture speed and peak slip-rate remain almost constant. Mean slip, peak slip-rate, and rupture speed decrease with increasing shear-zone half-width, whereas mean rise time increases. Shear-zone half-width distinctly affects the correlation between rupture parameters, especially for parameter pairs (slip, rupture speed), (peak slip-rate, rupture speed), and (rupture speed, rise time). Hydraulic diffusivity has negligible effects on these correlations. Variations in shear-zone half-width primarily impact rupture speed, which then may affect other rupture parameters. We find a negative correlation between slip and peak slip-rate, unlike simpler dynamic rupture models. Mean peak ground velocities decrease faster with increasing shear-zone half-width than with increasing hydraulic diffusivity, whereas ground-motion variability is similarly affected by both the parameters. Our results show that shear-zone half-width affects rupture dynamics, kinematic rupture properties, and ground shaking more strongly than hydraulic diffusivity. We interpret the importance of shear-zone half-width based on the characteristic time of diffusion. Our findings may inform pseudodynamic rupture generators and guide future studies on how to account for thermal-pressurization effects.

KEY POINTS

- We examine fluid thermal pressurization (TP) effects on earthquake rupture dynamics and ground motions.
- Shear-zone half-width has a stronger impact than hydraulic diffusivity on rupture dynamics and ground motions.
- Our findings inform future dynamic rupture simulation studies to account for TP effects.

Supplemental Material

INTRODUCTION

Most rocks in the upper crust are porous and hence may contain small amounts of fluids. Fault zones often are preferred paths for fluid transport in the crust. Pore fluids affect the stress and strain conditions of rocks before, during, and after an earthquake (Sibson, 1973, 1977, 1980; Lamb, 2006; Madden *et al.*, 2022). Frictional heat produced in the slip zone during

1. King Abdullah University of Science and Technology, Jeddah, Saudi Arabia, https://orcid.org/0000-0001-7199-1460 (JCV); https://orcid.org/0000-0002-9744-4964 (PMM); 2. Institute of Geophysics and Planetary Physics, Scripps Institution of Oceanography, University of California San Diego, La Jolla, California, U.S.A., https://orcid.org/0000-0003-0112-8412 (A-AG); 3. Department of Earth and Environmental Sciences, Ludwig-Maximilians-Universität München, Munich, Germany, https://orcid.org/0000-0002-4164-8933 (TU); 4. Geoazur Laboratory, Université Côte d'Azur, Valbonne, France, https://orcid.org/0000-0002-4827-7987 (J-PA)

*Corresponding author: jagdish.vyas@kaust.edu.sa

Cite this article as Vyas, J. C., A.-A. Gabriel, T. Ulrich, P. M. Mai, and J.-P. Ampuero (2023). How Does Thermal Pressurization of Pore Fluids Affect 3D Strike-Slip Earthquake Dynamics and Ground Motions? *Bull. Seismol. Soc. Am.* **XX**, 1–17, doi: 10.1785/0120220205

earthquake rupture may cause thermal expansion, flow, and pressurization of pore fluids that influence stress conditions on the fault and in the surrounding rocks (Sibson, 1973, 1980; Lachenbruch, 1980; Mase and Smith, 1984, 1987; Andrews, 2002). Thermal pressurization (TP) of pore fluids is thus an important dynamic weakening mechanism affecting earthquake rupture nucleation, propagation, and arrest.

The TP mechanism operates as follows: thermal expansion and confinement of fluids within a rock matrix of lower thermal expansivity produce a stark increase of pore fluid pressure. This decreases effective normal stress, which in turn lowers fault frictional strength, thereby enhancing fault dynamic weakening during earthquake rupture (Andrews, 2002; Bizzarri and Cocco, 2006a,b; Suzuki and Yamashita, 2006; Noda and Lapusta, 2010; Garagash, 2012; Viesca and Garagash, 2015; Brantut *et al.*, 2019; Badt *et al.*, 2020). The resulting reduction of fault strength may prevent coseismic melting and resolve the so-called heat-flow paradox (Lachenbruch and Sass, 1980; Andrews, 2002; Di Toro *et al.*, 2011; Acosta *et al.*, 2018; Badt *et al.*, 2020).

The TP effects may play a significant role in modulating the magnitude of induced or triggered earthquakes in georeservoirs, governed by pressure change and fluid flow (e.g., Galis *et al.*, 2017, 2019). Fluid-saturated clay-rich fault materials in subduction zone environments may promote earthquake rupture propagation and slip due to pressurization of pore fluid and low permeability of surrounding materials, resulting in dramatic dynamic weakening behavior and low breakdown work (Tinti *et al.*, 2005; Cocco *et al.*, 2006; Hirono *et al.*, 2016; Aretusini *et al.*, 2021). TP may also govern subduction dynamics, as suggested by geological signatures found in exhumed ancient subduction thrusts, including fluidization of comminuted material and an increase in the volume of fluid inclusions by frictional heating (Ujiie *et al.*, 2010). TP effects may lead to effective slip-weakening distances ranging from 0.03 to 0.22 m for subduction thrusts, which indicates high radiated energy and fast stress release (Ujiie *et al.*, 2010). TP may also explain why stable creeping parts of the fault become unstable during coseismic slip, as observed during the 2011 M_w 9.0 Tohoku Oki earthquake (Mitsui *et al.*, 2012; Noda and Lapusta, 2013).

Theoretical and numerical studies suggest that TP may also affect earthquake rupture properties such as stress drop and fracture energy. Andrews (2002) shows that the stress drop associated with TP rises with increasing rupture propagation distance and may eventually dominate over the frictional-induced stress drop. Recently, Perry *et al.* (2020) demonstrated that enhanced dynamic weakening due to TP is consistent with the observationally inferred magnitude invariance of stress drop. Simulations of earthquake sequences on rate-and-state faults with TP suggest that major faults operate at low overall shear stress levels, whereas the peak stress at the rupture front is consistent with static friction coefficients of 0.6–0.9 (Noda *et al.*, 2009). Viesca and Garagash (2015) hypothesize that TP may explain the observed distinct transition in the scaling of fracture energy with earthquake size, which implies different fault weakening processes for large and small earthquakes. Moreover, the seismologically inferred increase in fracture energy with earthquake magnitude may also be explained with TP (Abercrombie and Rice, 2005; Rice, 2006; Viesca and Garagash, 2015; Perry *et al.*, 2020). In simple dynamic earthquake rupture simulations, TP facilitates rupture propagation and activation of fault branches and increases rupture speed and slip rate (Urata *et al.*, 2014; Schmitt *et al.*, 2015).

Lambert *et al.* (2021) examined why large earthquakes occur at lower stress levels than their expected static strength using numerical seismic-cycle modeling. They tested two competing hypotheses: (1) faults are quasi-statically strong but experience significant weakening during earthquake rupture, and (2) faults are persistently weak because of pore fluid overpressure. They found that the former produces sharper self-healing pulse-like ruptures, larger dynamic stress changes, and larger radiated energy than that inferred for megathrust earthquakes, whereas the latter produces mildly crack-like ruptures. Therefore, their findings suggest two possibilities: either large earthquakes do not propagate as self-healing pulses, or the radiated energy is substantially underestimated for megathrust earthquakes. Their results raise questions about earthquake rupture physics for large events and their weakening mechanisms.

Acosta *et al.* (2018) performed laboratory experiments to investigate the role of flash heating and TP on the dynamic weakening of faults. They observed that loss in fault strength is due to flash heating under dry and low pressure (1 MPa) conditions, whereas at high fluid pressure (25 MPa) flash heating is inhibited, and TP becomes important. Badt *et al.* (2020) tested the mechanical response of faults under elevated, confining pore pressures in laboratory experiments, and suggest that the magnitude and rate of weakening increases as the sample permeability decreases with limited frictional heat production. Their experiments support the hypothesis that TP is an active dynamic weakening mechanism during earthquake rupture at least in the early stages of fault slip.

Seismic radiation and near-field ground-motion characteristics depend on earthquake rupture dynamics. Observations of strong ground motions show intricate variations depending on parameters like source-to-site distance, earthquake magnitude and faulting style, hypocenter position, azimuth with respect to fault plane and rupture direction, and others (Youngs *et al.*, 1995; Rodriguez-Marek *et al.*, 2011; Imtiaz *et al.*, 2015; Vyas *et al.*, 2016; Gallovič, 2017; Crempien and Archuleta, 2018). We are here interested in how TP may modulate the amplitudes and spectral properties of near-fault ground motions. For instance, a higher spectral velocity response at long periods (~10 s) was observed at receivers near the northern portion of the main fault of the 1999 M_w 7.6 Chi–Chi, Taiwan, earthquake, compared to recordings at receivers near the southern portion of fault, has been attributed to TP (Andrews, 2005).

Correspondingly, we examine the effect of TP on rupture dynamics and ground-motion properties.

Two numerical modeling approaches, kinematic and dynamic rupture modeling, can be used to simulate ground shaking. In kinematic rupture modeling the spatiotemporal evolution of the rupture process is specified, whereas in dynamic rupture modeling the rupture is allowed to evolve in a self-consistent manner based on fault stress and frictional conditions. Dynamic rupture simulations are computationally more expensive than kinematic simulations. An alternative is to use pseudodynamic rupture models, which are kinematic models that emulate physical characteristics consistent with dynamic rupture modeling. Pseudodynamic models are developed based on the correlation between kinematic rupture parameters, for example, correlations between slip and rise time, or slip and rupture speed (e.g., Guatteri *et al.*, 2003; Mena *et al.*, 2012). However, thus far correlations among these kinematic rupture parameters have been analyzed without incorporating TP (e.g., Oglesby and Day, 2002; Guatteri *et al.*, 2003; Schmedes *et al.*, 2010, 2013; Song *et al.*, 2014; Mai *et al.*, 2018). Therefore, a detailed analysis of how TP affects kinematic rupture parameters and their correlations can advance pseudodynamic rupture modeling.

In our study, we focus on a systematic investigation to quantitatively understand how TP affects kinematic rupture properties and hence near-field ground motions. In so doing, we aim to better constrain rupture physics and ground-motion characteristics. For example, TP parameters that control slip and rupture speed may control rupture directivity effects, leading to potentially higher near-field ground-shaking variability for unilateral ruptures (Vyas *et al.*, 2016). Understanding TP effects on peak slip rates (PSRs) will provide insights into ground-motion amplitudes. By developing an understanding of how TP parameters govern rupture dynamics, kinematic rupture properties, and ground-motion behavior for earthquakes in fluid-rich environments, we help advance future simulation studies.

Numerical implementations that include TP in dynamic earthquake rupture modeling are based on the theoretical foundations of the conservation of fluid mass and energy, Fourier's law, and Darcy's law (Andrews, 2002; Bizzarri and Cocco, 2006a,b; Noda *et al.*, 2009; Noda and Lapusta, 2010; Schmitt *et al.*, 2015). However, no joint investigation exists on how TP may influence dynamic and kinematic properties and ground-motion characteristics associated with earthquake rupture. In this study, we perform a parametric sensitivity analysis using 3D dynamic rupture modeling with a strong velocity-weakening rate-and-state friction law and TP to quantify the influence of TP on kinematic rupture characteristics, such as fault slip, PSR, rupture speed (V_r), and rise time (T_r). We also examine how TP alters correlations among these kinematic rupture parameters. In addition, we investigate the effects of TP on earthquake ground-motion properties.

COMPUTATIONAL METHOD AND MODEL SETUP

We perform 3D dynamic rupture modeling of strike-slip earthquakes accounting for TP. The 3D benchmark problem treated by Ulrich *et al.* (2020) forms the basis for these simulations. In this section, we provide details on the fault friction law, the TP model, the numerical method, and the parameter space explored.

Frictional properties

Past laboratory experiments on rocks and metals, as well as theoretical studies, suggest that friction depends on slip rate and state of the contact surface (Rabinowicz, 1958, 1959; Dieterich, 1972, 1978, 1981; Ruina, 1980, 1983; Gu *et al.*, 1984; Gu, 1984, 1986). The Dieterich–Ruina rate-and-state friction law (Dieterich, 1981; Ruina, 1983) has been used to explain earthquake dynamic processes, stick–slip behavior of earthquakes, accelerated creep preceding slip events in a stick–slip system, foreshocks, and aftershocks (Dieterich and Kilgore, 1996; Scholz, 1998; Ampuero and Rubin, 2008; Grzemba, 2015). The compact form of the Dieterich–Ruina friction law is

$$f(V,\Psi) = f_0 + a\log(V/V_0) + b\log(\Psi V_0/D_c). \quad (1)$$

In equation (1), the friction coefficient f depends on slip rate V and state variable Ψ; f_0 and V_0 are the reference friction coefficient and the slip rate, respectively. Constitutive parameters a, b, and D_c are determined in laboratory experiments. The steady-state friction coefficient Ψ_{SS} is a function of a–b. Ψ_{SS} increases if a–b is positive leading to velocity-strengthening behavior, whereas it decreases for negative a–b causing velocity-weakening of friction.

The previous formulation of rate-and-state friction is determined in laboratory experiments at subseismic slip rates ($V < 1$ cm/s). Therefore, its extrapolation to earthquake conditions needs to be further examined. A recent study by Spagnuolo *et al.* (2016) proposed a modified rate-and-state friction law for subseismic to seismic slip rates (0.1 μm/s < $V < 3$ m/s) based on a large published and unpublished experimental dataset. They found that the steady-state friction coefficient has a strong negative dependence on slip rate at high velocity ($V > 1$ cm/s) for three rock types under consideration. Velocity-weakening friction faults under different loading conditions may result in different rupture behavior: self-healing pulses or crack-like rupture (e.g., Zheng and Rice, 1998). Our dynamic rupture simulations account for large frictional weakening and have stress conditions that give rise to rupture as self-healing pulses.

We adopt a strong velocity-weakening rate-and-state friction law (Dunham *et al.*, 2011) that replicates the large friction reduction observed in laboratory experiments at coseismic slip rates (Di Toro *et al.*, 2011). The fault's shear strength is a product of the friction coefficient f and the effective normal stress $\overline{\sigma}$:

$$\tau = f(V,\Psi)\overline{\sigma}. \quad (2)$$

The friction coefficient is a function of slip velocity (V) and a state variable (Ψ):

$$f(V,\Psi) = a\sinh^{-1}\left[\frac{V}{2V_0}\exp\left(\frac{\Psi}{a}\right)\right]. \quad (3)$$

The state variable evolves according to the following equation:

$$\frac{d\Psi}{dt} = -\frac{V}{L}\left[\Psi - \Psi_{SS}(V)\right], \quad (4)$$

in which the steady-state value of the state variable is

$$\Psi_{SS}(V) = a\ln\left\{\frac{2V_0}{V}\sinh\left[\frac{f_{SS}(V)}{a}\right]\right\}. \quad (5)$$

The steady-state friction coefficient f_{SS} depends on V as

$$f_{SS}(V) = f_w + \frac{f_{LV}(V) - f_w}{[1 + (V/V_w)^8]^{1/8}}, \quad (6)$$

with a low-velocity steady-state friction coefficient given by

$$f_{LV}(V) = f_0 - (b-a)\ln(V/V_0). \quad (7)$$

The steady-state friction coefficient f_{SS} approaches the low-velocity steady-state friction coefficient f_{LV} at low slip rates ($V \ll V_w$ in equation 6) and approaches the fully weakened friction coefficient f_w at high slip rates ($V \gg V_w$). Laboratory experiments indicate that f_w and V_w have values near 0.2 and 0.1 m/s, respectively (e.g., Di Toro *et al.*, 2004; Beeler *et al.*, 2008). The reference friction coefficient (f_0), reference slip velocity (V_0), direct effect parameter (a), state evolution effect parameter (b), fully weakened friction coefficient (f_w), weakening slip velocity (V_w), and state evolution distance (L) are chosen constant over the central portion of the fault, a rectangular velocity-weakening asperity (see Fig. 1, Table 1). The frictional behavior then transitions to velocity-strengthening in the surrounding region (Fig. 1a) over a transition zone with a width (h) of 3 km, which allows a gradual arrest of the rupture in our simulations. Rupture is inhibited by increasing the direct-effect parameter to $a + \Delta a_0$ and the weakening slip velocity to $V_w + \Delta V_{w0}$ via the following spatial distributions:

$$\Delta a(x,z) = \Delta a_0[1 - B_1(x;H,h)\ B_2(z;H,h)], \quad (8)$$

$$\Delta V_w(x,z) = \Delta V_{w0}[1 - B_1(x;H,h)\ B_2(z;H,h)], \quad (9)$$

in which

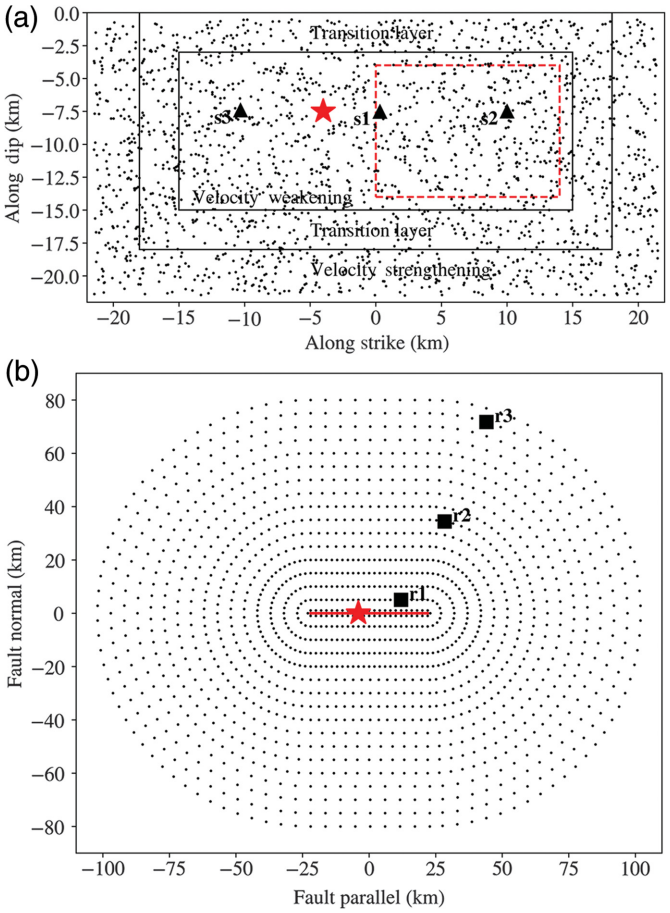

Figure 1. (a) On-fault receivers at which rupture parameters are evaluated. Black dots mark receivers used in the statistical analysis, and the three triangles (*s*1, *s*2, and *s*3) denote receivers at which we analyze the detailed temporal evolution of rupture parameters. Receivers inside the red dashed rectangle are used for analyzing correlations of rupture parameters. (b) Receiver array at the Earth's surface for ground-motion analysis. Black dots mark receivers used in the statistical analysis, and the three squares (*r*1, *r*2, and *r*3) are receivers used for analyzing ground velocity time histories.

$$B_1(x;H,h) = \begin{cases} 1, & |x| \le H \\ 0.5\left[1 + \tanh\left(\frac{h}{|x|-H-h} + \frac{h}{|x|-H}\right)\right], & H < |x| < H+h, \\ 0, & |x| \ge H+h \end{cases} \quad (10)$$

$$B_2(z;H,h) = \begin{cases} 0.5\left[1 + \tanh\left(\frac{h}{h-z} - \frac{h}{z}\right)\right], & z < h \\ 1, & h \le z \le H \\ 0.5\left[1 + \tanh\left(\frac{h}{z-H-h} + \frac{h}{z-H}\right)\right], & H < z < H+h \\ 0, & z \ge H+h \end{cases}. \quad (11)$$

In equations (8)–(11), (x, y, z) defines a right-handed coordinate system in which x is the strike direction, and z is in the

TABLE 1
Modeling Parameters and Physical Characteristics

	Variable	Notation	Value
Material properties			
	P-wave velocity	c_P	5.901 km/s
	S-wave velocity	c_S	3.407 km/s
	Density	ρ	2760 kg/m^3
Frictional properties			
	Steady-state friction coefficient	f_0	0.6
	Reference slip velocity	V_0	1 μm/s
	Direct effect parameter	a	0.01
	State evolution effect parameter	b	0.014
	Fully weakened friction coefficient	f_w	0.25
	Weakening slip velocity	V_w	0.15 m/s
	State evolution distance	L	0.4 m
TP properties			
	Thermal diffusivity	α_{th}	1×10^{-6} m^2/s
	Volumetric heat capacity	ρc	2.7 MJ/m^{3}K
	Pore-pressure increase per unit temperature	Λ	0.1 MPa/K
	Hydraulic diffusivity	α_{hy}	(15, 18, 21, 24, 27, 30, 33) $\times 10^{-5}$ m^2/s
	Shear-zone half-width	w	15, 18, 21, 24, 27, 30, 33 mm

vertical upward direction, such that $x = 0$ is in the center of the fault and $z = 0$ at the Earth surface. We assume $H = 15$ km, $h = 3$ km, $\Delta a_0 = 0.01$, and $\Delta V_{w0} = 0.95$ for all simulations presented in this study.

Implementation of TP

To include TP effects in dynamic rupture simulations, we solve the 1D diffusion equations for temperature (T) and pore pressure (p) in the direction normal to the fault (Noda and Lapusta, 2010):

$$\frac{\partial T}{\partial t} = \alpha_{th}\frac{\partial^2 T}{\partial y^2} + \frac{\tau V}{\rho c w\sqrt{2\pi}}\exp\left(\frac{-y^2}{2w^2}\right), \tag{12}$$

$$\frac{\partial p}{\partial t} = \alpha_{hy}\frac{\partial^2 p}{\partial y^2} + \Lambda\frac{\partial T}{\partial t}, \tag{13}$$

in which α_{th} is the thermal diffusivity, ρc is the volumetric heat capacity, τ is the shear strength, V is the slip velocity, w is the shear-zone half-width, α_{hy} is the hydraulic diffusivity, and Λ is the pore pressure increase per unit increase in temperature. The above TP formulation does not include porosity evolution, which would affect pore pressure changes, and hence rupture dynamics and resulting stress drop (Mitsui and Cocco, 2010). The above 1D TP approximation is valid, because dynamic rupture time scales are short compared to the time scales of diffusion along the fault (Zhu *et al.*, 2020). We follow Noda and Lapusta (2010), Noda *et al.* (2009), and Andrews (2002) in assuming that the shear strain rate has a Gaussian profile in the fault-normal direction, whereas Bizzarri and Cocco (2006a,b) assumed a uniform profile.

We define α_{hy} to be constant in the velocity-weakening region and to increase by $\Delta\alpha_{hy}$ in the velocity-strengthening region, with the following spatial distribution:

$$\Delta\alpha_{hy}(x,z) = \Delta\alpha_{hy0}[1 - B_1(x;H,h)\ B_3(z;H,h)], \tag{14}$$

in which $\Delta\alpha_{hy0} = 1$ m^2/s and

$$B_3(z;H,h) = \begin{cases} 1, & z \le H \\ 0.5\left[1 + \tanh\left(\frac{h}{z-H-h} + \frac{h}{z-H}\right)\right], & H < z < H + h. \\ 0, & z \ge H + h \end{cases} \tag{15}$$

Laboratory experiments and the previous dynamic rupture simulations accounting for TP suggest that α_{hy} ranges from 10^{-5} to 10^{-2} m^2/s and w ranges from 1 to 100 mm (Kranz *et al.*, 1990; Andrews, 2002; Wibberley, 2002; Wibberley and Shimamoto, 2005; Noda *et al.*, 2009; Noda and Lapusta, 2010; Schmitt *et al.*, 2015; Perry *et al.*, 2020; Lambert *et al.*, 2021). Here, we vary the values of both parameters as indicated in Table 1. The chosen ranges of α_{hy} and w (Table 1) ensure that ruptures propagate over the entire fault and remains mostly at subshear speeds (with only localized supershear rupture episodes). Rupture is arresting smoothly. Our parameter choices provide realistic rupture processes across all simulations and prevent unphysically high temperatures ($T > 1200$ K).

We conducted 49 dynamic rupture simulations considering seven different values for α_{hy} and w (Table 1), respectively. The initial on-fault shear stress distribution and nucleation procedure are described in Appendices A and B of the supplemental material available to this article.

Numerical method and discretization

We use the open-source software SeisSol, which is based on the Arbitrary high-order accurate DERivative Discontinuous Galerkin (ADER-DG) method (Dumbser and Käser, 2006; Pelties *et al.*, 2014; Uphoff *et al.*, 2017), to solve the coupled dynamic rupture and 3D wave propagation problem including TP effects. We use a fourth-order accurate numerical scheme with basis functions of polynomial order 3. The fault is planar and of size 44 km × 22 km. The computational domain is set to be 220 km × 180 km × 40 km and discretized using an unstructured mesh of 13.6 million tetrahedral elements. Element edge lengths are 1500 m over most of the domain but refined to 200 m close to the fault. We consider a uniform Earth structure with constant *P*- and *S*-wave velocities (Table 1). Our simulations resolve the seismic wavefield for frequencies up to $f_{\max} = 3.5$ Hz close to the fault and ≈0.5 Hz in the more coarsely meshed regions. We store rupture parameters at 2000 randomly distributed on-fault receivers (Fig. 1a) and ground velocity time series at 1516 surface receivers distributed along a range of Joyner–Boore distances (R_{JB}, Fig. 1b). With these settings, simulating 55 s of rupture process and wave propagation requires around 3.6 hr on 256 × 64 Haswell cores of the Shaheen II supercomputer at King Abdullah University of Science and Technology (KAUST).

A spectral implementation of TP for 3D discontinuous Galerkin dynamic rupture methods

Implementations of TP for dynamic rupture modeling vary in efficiency and flexibility. Explicit finite difference (FD) schemes are straightforward to implement and allow for heterogeneous properties, such as diffusivity, within the bulk. Noda *et al.* (2009) discretized spatial derivatives on a 1D grid orthogonal to the fault using a central difference scheme and time derivatives using an explicit Euler scheme. However, such FD methods require small time steps and large memory due to the interpolation between major time steps, which involves storing the slip history at all subtime steps. The spectral method (Noda and Lapusta, 2010) allows for larger timesteps, has small numerical errors, and is memory efficient. Although it is restricted to homogeneous TP parameters along the direction normal to the fault, the spectral implementation has the advantage of exploiting the symmetry of the diffusion equation for similar material parameters on both the sides of the fault.

Here, we couple the semianalytic, stable, precise, and efficient spectral diffusion solver of Noda and Lapusta (2010) with 3D dynamic rupture modeling in the high performance computing enabled ADER-DG software SeisSol. The diffusion solver uses a truncated Fourier expansion to evaluate the second-order space derivatives. The approximation due to truncation is very accurate; the heat source is assumed to have a Gaussian profile, and the Fourier spectrum of a Gaussian decays rapidly. We first precalculate the inverse Fourier coefficients using a trapezoidal rule. Next, we calculate the current shear stresses and slip, and then the shear-generated heat in the spectral domain. In the next timestep, temperature and pressure are updated in the wavenumber domain. Finally, we recover temperature and pore pressure in the space domain by inverse Fourier transformation using the precalculated coefficients.

In contrast to finite-element (FE) methods, the basis functions here are nonzero over the entire domain leading to a global approach. We implement the update scheme for this TP solver coupled to strongly rate-dependent friction dynamic rupture following Kaneko *et al.* (2008). We observe lower computational overhead when comparing SeisSol's spectral TP implementation to an FE TP approach and comparable computational overhead to an FD TP solver, in comparison to respective SeisSol, finite element method, or FD simulations without TP. Similar to Noda and Lapusta (2010), we assume for simplicity that the heat source remains constant during each timestep. Li and Greengard (2007) show how to construct a fourth-order accurate spectral method for the heat equation, which may be an interesting avenue for future TP implementations in dynamic rupture solvers.

Verification of the 3D TP implementation in SeisSol

Although analytical solutions are available for a shear-heating zone of zero thickness (Rice, 2006) or for a short-term constant heat input under constant slip rate (Noda and Lapusta, 2010), more complex 3D dynamic rupture simulations with TP have to be verified without available analytical references. We verify our 3D TP implementation in SeisSol following the most recent Southern California Earthquake Center (SCEC) dynamic rupture community benchmark TPV105-3D (Harris *et al.*, 2011, 2018; Gabriel *et al.*, 2020). Conducting an earlier 2D TP benchmark (TPV105-2D from 2011; Harris *et al.*, 2018) revealed important physical challenges, such as the occurrence of high temperatures implying widespread frictional melting and numerical challenges, including lack of accuracy and large differences between results with different time integration schemes.

We compare the SeisSol solution for the TPV105-3D benchmark with two alternative TP-enabled dynamic rupture codes. Figure 2 shows a comparison of horizontal shear stress and slip rates computed with FaultMod, SeisSol, and Support Operator Rupture Dynamics (SORD), which use different numerical schemes (FE, ADER-DG, and generalized FD, respectively). The SeisSol solution (JV) achieves excellent agreement with FaultMod (MB) and SORD (YW; Fig. 2).

The above 3D benchmark settings form the basis of our subsequent rupture simulations. The benchmark setup (Ulrich *et al.*, 2020) describes a narrow parameter range (with respect to observational uncertainties) to define realistic earthquake ruptures on a single, planar fault. It includes a velocity-strengthening transition layer at shallow depths to limit

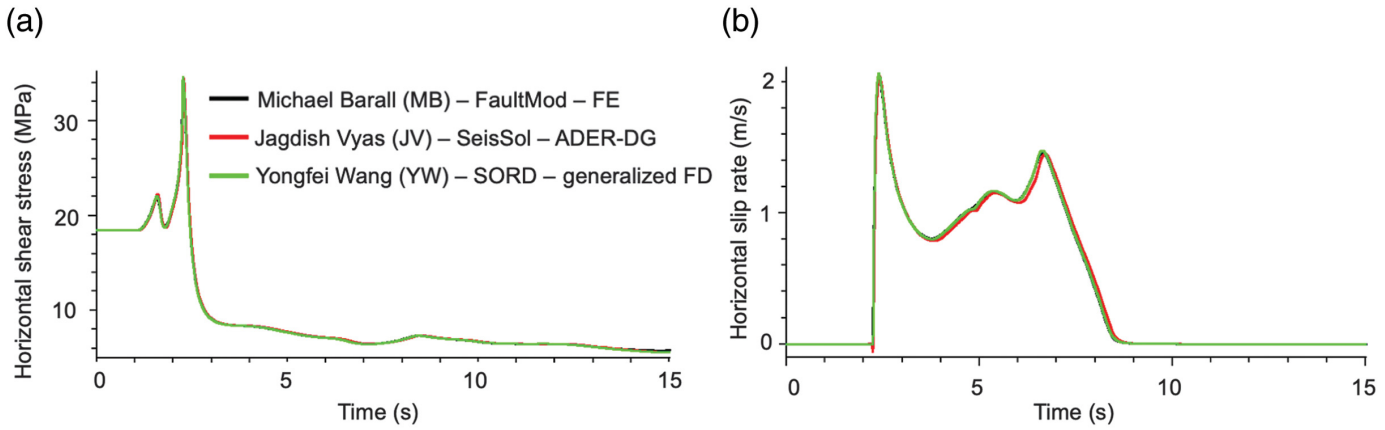

Figure 2. Comparison of the temporal evolution of along-strike (horizontal) (a) shear stress and (b) slip rate at a given fault location, computed using three different numerical methods as part of the Southern California Earthquake Center (SCEC) TPV105-3D benchmark exercise for validating dynamic rupture codes.

localized supershear rupture speeds and spatially varying hydraulic diffusivity correlated with the rate-and-state parameters for smooth rupture stopping to generate realistic ground motions. The frictional-strengthening behavior at shallow depths is supported by seismicity observations; the depth distribution of seismicity indicates that earthquake nucleation is less probable at depths shallower than 2–4 km, suggesting a positive slip-rate dependence of frictional resistance (velocity strengthening) at these depths (Marone and Scholz, 1988; Scholz, 2019; Verberne *et al.*, 2019). The chosen TP-parameter values prevent unrealistically high temperatures ($T > 1200$ K) that would imply melting. For example, the melting temperatures of granite and basalt are around 1500 K and 1300 K, respectively. The model features spatially heterogeneous TP characteristics, prevents high frictional heat, and sets shear traction at 49% of normal traction. Designing a physically plausible 3D benchmark was challenging due to the strong trade-offs of rupture nucleation, smooth rupture termination without reaching fault ends, rapid dynamic weakening effects, and realistic heat production. Therefore, our dynamic rupture modeling setup here closely resembles the TPV105-3D benchmark.

TP INFLUENCE ON RUPTURE CHARACTERISTICS AND GROUND SHAKING

Next, we statistically analyze the effects of TP on the temporal evolution of kinematic source parameters and ground-motion velocities.

Rupture parameter evolution and statistics

We analyze the temporal evolution of rupture parameters as a function of TP parameters. Figure 3 shows the effects of varying hydraulic diffusivity α_{hy} (in meter squared per second) and shear-zone half-width w (in millimeters) on the temporal evolution of along-strike slip rate (SRs), total traction ($Ts0$), temperature (T), and pore pressure (Pf) at location $s2$ on the fault (Fig. 1a). We observe a stronger influence of w on slip rates, $Ts0$, T, and Pf compared to α_{hy}. The onset time of rupture is delayed as we increase w but remains almost unaffected when varying α_{hy}. Similarly, the absolute peak values of slip rate, temperature, and pore pressure decreases more rapidly when increasing w than when increasing α_{hy}. The dependence of these kinematic source properties on TP parameters at two alternative fault locations ($s1$ and $s3$) shows similar characteristics as observed at $s2$ (compare Figs. S1 and S2 with Figure 3).

We further quantify the effects of TP on the earthquake source process by statistically analyzing kinematic rupture properties for 2000 on-fault receivers. We first analyze the mean values of slip, PSR, V_r, and T_r. To evaluate rupture speed (V_r), we first measure the rupture onset time T at each fault point, defined as the time at which slip rate exceeds 1 mm/s. We then compute V_r as $1/\|\nabla(T)\|$, using 2D basis functions across each fault element face. Figure 4 shows variations in mean slip, PSR, V_r, and T_r for varying α_{hy} for a given w (color coded). Mean slip and T_r decrease almost 10% and 6%, respectively, as we double the value of α_{hy} for a given w, whereas PSR and V_r remain nearly constant. With increasing α_{hy}, the fluid diffuses faster, leading to faster pore pressure reduction behind the rupture front. This, in turn, increases effective normal stress and therefore restrengthens the fault, favoring self-healing, which thus explains the observed reduced fault slip and rise time with increasing α_{hy}. The fault-slip reduction translates into a drop of earthquake magnitude M_w of about 0.03 magnitude units when doubling α_{hy} (Fig. S3).

Let us now examine the effects of w on kinematic rupture properties and compare with α_{hy}. Figure 5 shows variations in mean slip, PSR, V_r, and T_r for varying w and fixed α_{hy}. Mean slip, PSR, and V_r decrease with increasing w, whereas mean T_r increases. Mean slip decreases by almost 10%, whereas mean T_r increases by almost 6% as w is doubled, similar to the changes found by varying α_{hy}. Hence, both α_{hy} and w almost

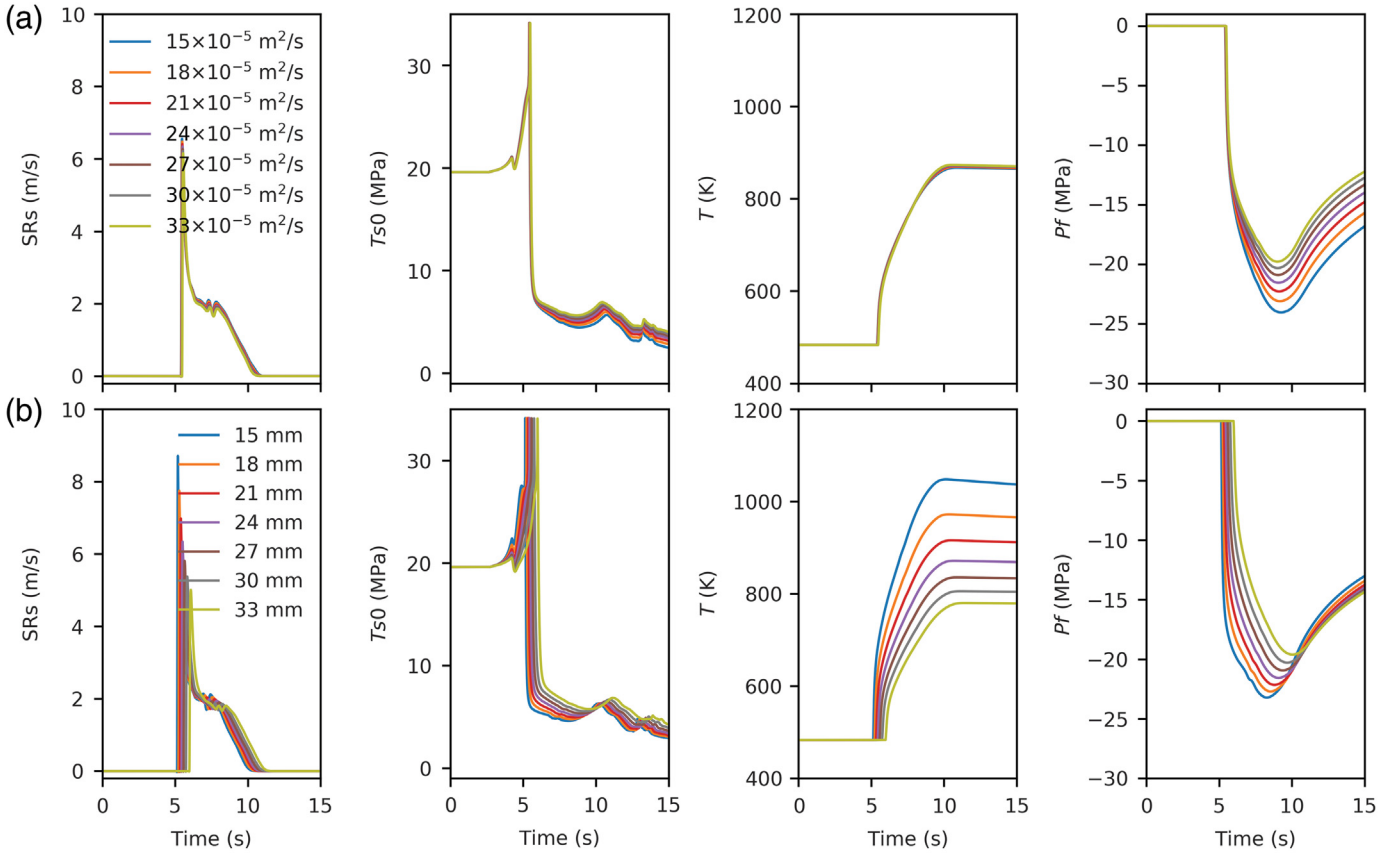

Figure 3. Temporal evolution of along-strike slip rate (SRs), shear traction along strike (*Ts*0), temperature (*T*), and fluid pressure (*Pf*) at receiver *s*2 (Fig. 1) for varying (a) hydraulic diffusivity α_{hy} and (b) shear-zone half-width *w*.

equally influence mean slip and earthquake magnitude (Fig. S3). Both the parameters have a similar effect on mean T_r but with opposite trends (decreasing and increasing, respectively). Mean PSR and V_r decrease by almost 60% and 14%, respectively, for doubled *w*, but are nearly unaffected by variations of α_{hy} in the considered range (Fig. 4). Therefore, *w* has a stronger impact than α_{hy} on the overall earthquake rupture process, particularly on PSR that strongly affects near-source ground motions.

Correlation of kinematic rupture parameters

Potential correlations between kinematic earthquake rupture parameters are important for pseudodynamic source modeling. Therefore, we examine the correlations between pairs of rupture parameters by calculating the Pearson correlation coefficient *r* between six pairs of source parameters: (slip, PSR); (slip, V_r); (slip, T_r); (PSR, V_r); (PSR, T_r); and (V_r, T_r). The linear correlation coefficient *r* does not completely capture potential nonlinear correlations, but *r* is considered by Schmedes *et al.* (2010), which thus allows us to compare our simulation results with theirs. As Schmedes *et al.* (2010), we exclude on-fault receivers around the rupture nucleation and arrest areas, by considering only receivers contained in the red dashed rectangle of Figure 1.

The correlation coefficients *r* between kinematic rupture parameters, shown as a function of varying hydraulic diffusivity α_{hy} for given shear-zone half-width *w* (Fig. 6), reveal limited

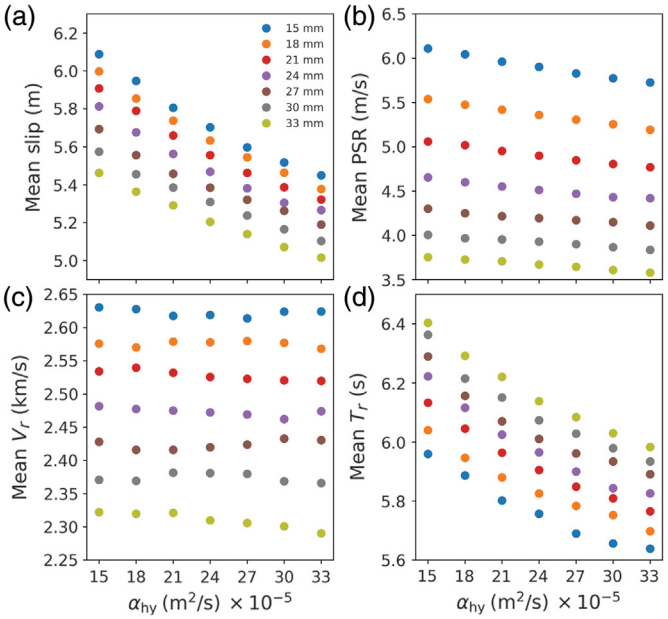

Figure 4. (a) Mean slip, (b) peak slip rate (PSR), (c) rupture speed (*Vr*), and (d) rise time (T_r) plotted with respect to hydraulic diffusivity α_{hy} for given shear-zone half-width *w* (color coded).

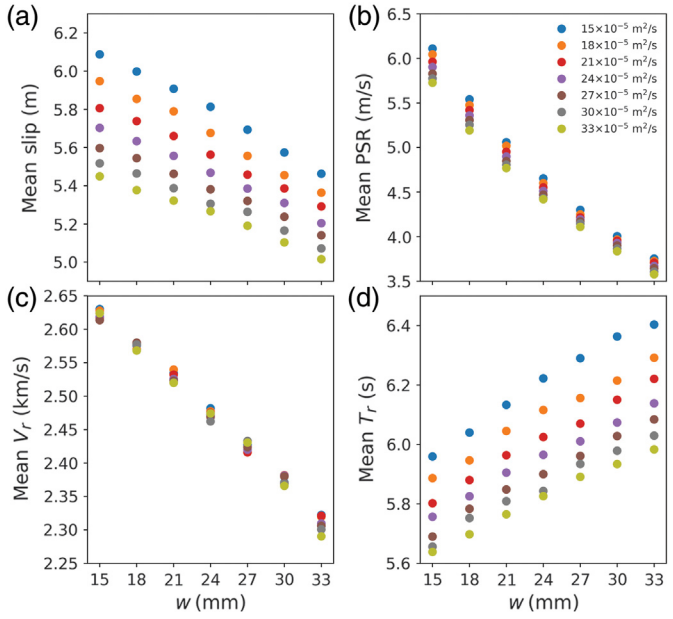

Figure 5. (a) Mean slip, (b) PSR, (c) rupture speed (V_r), and (d) rise time (T_r) displayed with respect to shear-zone half-width w for given hydraulic diffusivity α_{hy} (color coded).

sensitivity to changes in α_{hy}. The pairs (slip, PSR) and (V_r, T_r) are negatively correlated ($r \sim -0.5$), and the pair (PSR, T_r) is strongly negatively correlated ($r \sim -1.0$). The pairs (slip, T_r) and (PSR, V_r) are positively correlated ($r \sim 0.5$), whereas (slip, V_r) is almost uncorrelated ($r \sim -0.2$). However, these r values do not vary much with respect to changes in hydraulic diffusivity α_{hy}.

In contrast, variations in shear-zone half-width w exert distinct changes in the correlation coefficient for specific source-parameter pairs. Figure 7 shows correlations among rupture parameters with varying w for fixed α_{hy}. Correlations among (slip, PSR), (slip, T_r), and (PSR, T_r) are essentially insensitive to changes in w, similar to what Figure 6 displays for varying α_{hy}. However, the (PSR, V_r) correlation increases from 0.3 to almost 0.7, whereas the (V_r, T_r) negative correlation increases from −0.3 to almost −0.7 when doubling w. The contribution of TP to dynamic weakening is substantial for the smallest explored w. Indeed, TP effects strongly decrease the correlation among (PSR, V_r) and (V_r, T_r). We also find a slight increase in negative correlation from −0.1 to −0.3 for (slip, V_r) when doubling w. All parameter pairs whose correlation increases with increasing w involve rupture speed V_r. This suggests that w may primarily affect V_r, which in turn may influence other kinematic source parameters (slip, PSR, and T_r).

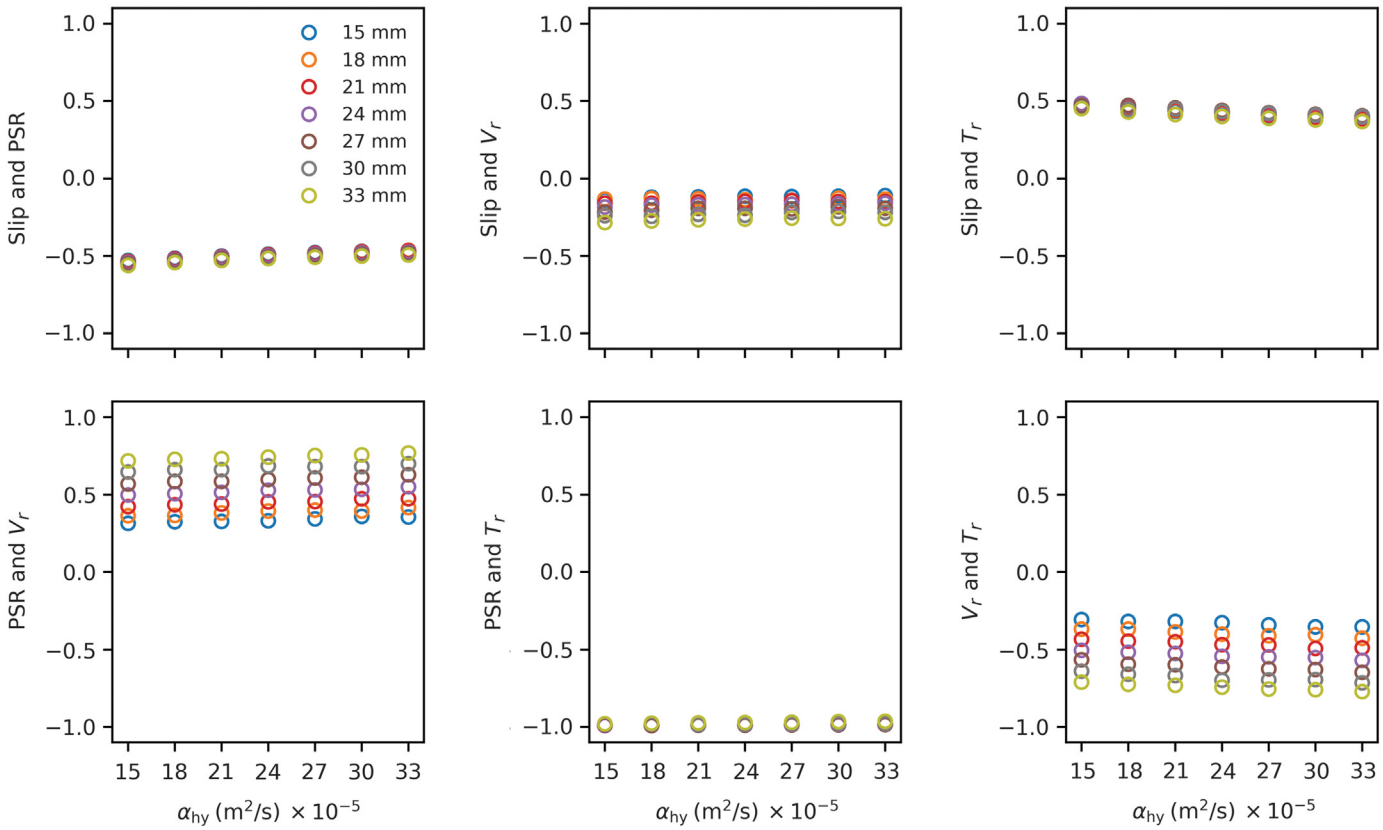

Figure 6. Correlations between rupture parameters as a function of α_{hy} for given w (color coded). Correlations are based on the set of receivers contained in the red dashed rectangle in Figure 1.

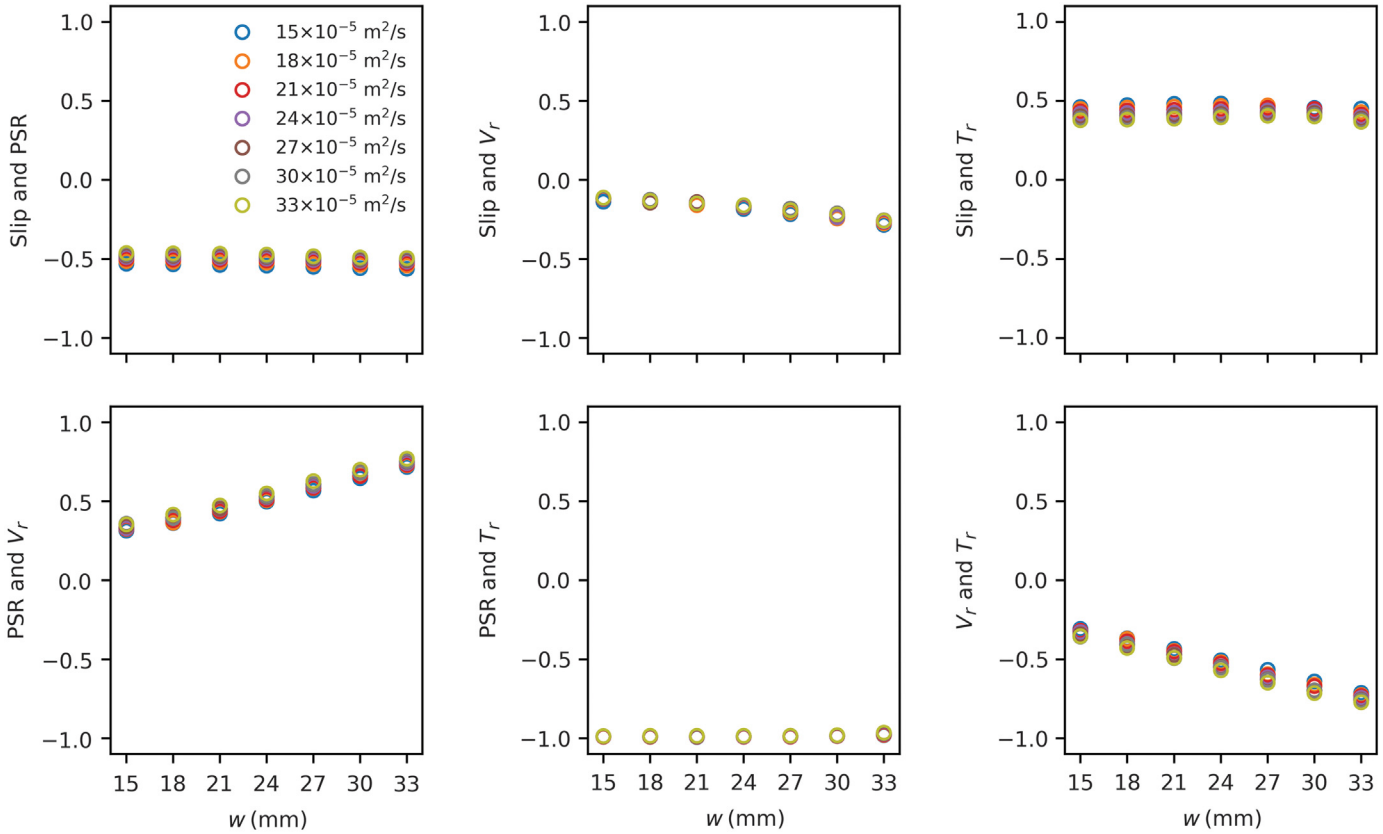

Figure 7. Correlations between rupture parameters as a function of w for given color-coded α_{hy}. Correlations are based on the set of receivers contained in the red dashed rectangle in Figure 1.

To further investigate the overall correlations among slip, PSR, V_r, and T_r, we compute mean values of rupture parameters considering all 49 models and each on-fault receiver. Figure 8 reveals that slip and PSR are negatively correlated ($r \sim -0.5$), which is in contrast to the positive correlation reported by Schmedes *et al.* (2010). However, the low correlation we observe between slip and V_r is consistent with findings of Schmedes *et al.* (2010). And the positive correlation for (slip, T_r; $r \sim 0.4$) is in agreement with the relation reported by Schmedes *et al.* (2010) with $r \sim 0.6$–0.7. We find that the PSR and V_r are positively correlated, whereas negative correlations appear for (PSR, T_r; $r \sim -1.0$) and (V_r, T_r; $r \sim -0.6$), consistent with findings reported by Schmedes *et al.* (2010) ($r \sim -0.2$ for the two negatively correlated pairs).

Importantly, the theoretical nonlinear relation between PSR and V_r derived in Gabriel *et al.* (2013) matches our simulation results (Fig. 8). The slightly different scaling factor between PSR and V_r estimated from our models (0.8) compared to the theoretical estimates (0.65) is due to 2D dynamic rupture modeling without TP by Gabriel *et al.* (2013).

The differences observed in correlation among rupture parameters in our study with respect to Schmedes *et al.* (2010) may be attributed to different assumptions and parameterizations in their rupture modeling regarding initial shear stress, friction law, and TP. We use depth-dependent initial shear stress (see Appendix A of supplemental material), whereas Schmedes *et al.* (2010) assume a spatially random heterogeneous initial shear stress with power-law spectral decay. They employ linear slip-weakening friction, whereas we use rate-and-state friction with strong velocity weakening. Our simulations also account for TP, whereas Schmedes *et al.* (2010) did not consider TP.

Ground velocity comparison and PGV statistics

One of the goals of this study is to understand if TP affects near-source ground motions, addressing the question if such detailed rupture physics may be relevant for seismic hazard applications. Therefore, we analyze ground velocity time series as a function of TP parameters. Figure 9 compares three-component ground velocity waveforms for three values of α_{hy} (15, 24, 33×10^{-5} m^2/s), and w (15, 24, 33 mm) at receivers $r1$–$r3$ (Fig. 1b). Velocity waveforms remain essentially unaffected by changes in α_{hy}. When increasing w, delayed first-arrival times and reduced peak amplitude can be observed; yet, waveform shapes remain unaltered (Fig. 9b). For example, the first arrival is delayed by nearly 0.7 s, and peak amplitudes are reduced by ≈30% on the fault-parallel component at receiver $r1$ as w increases by a factor of 2 (from 15 to 33 mm). Hence, variations in w affect ground-motion velocities, but α_{hy} has little effect.

To quantify the effects of w and α_{hy} on ground-motion amplitude, we compute the mean and standard deviation of peak ground velocity (PGV) for all receivers at a given Joyner–Boore

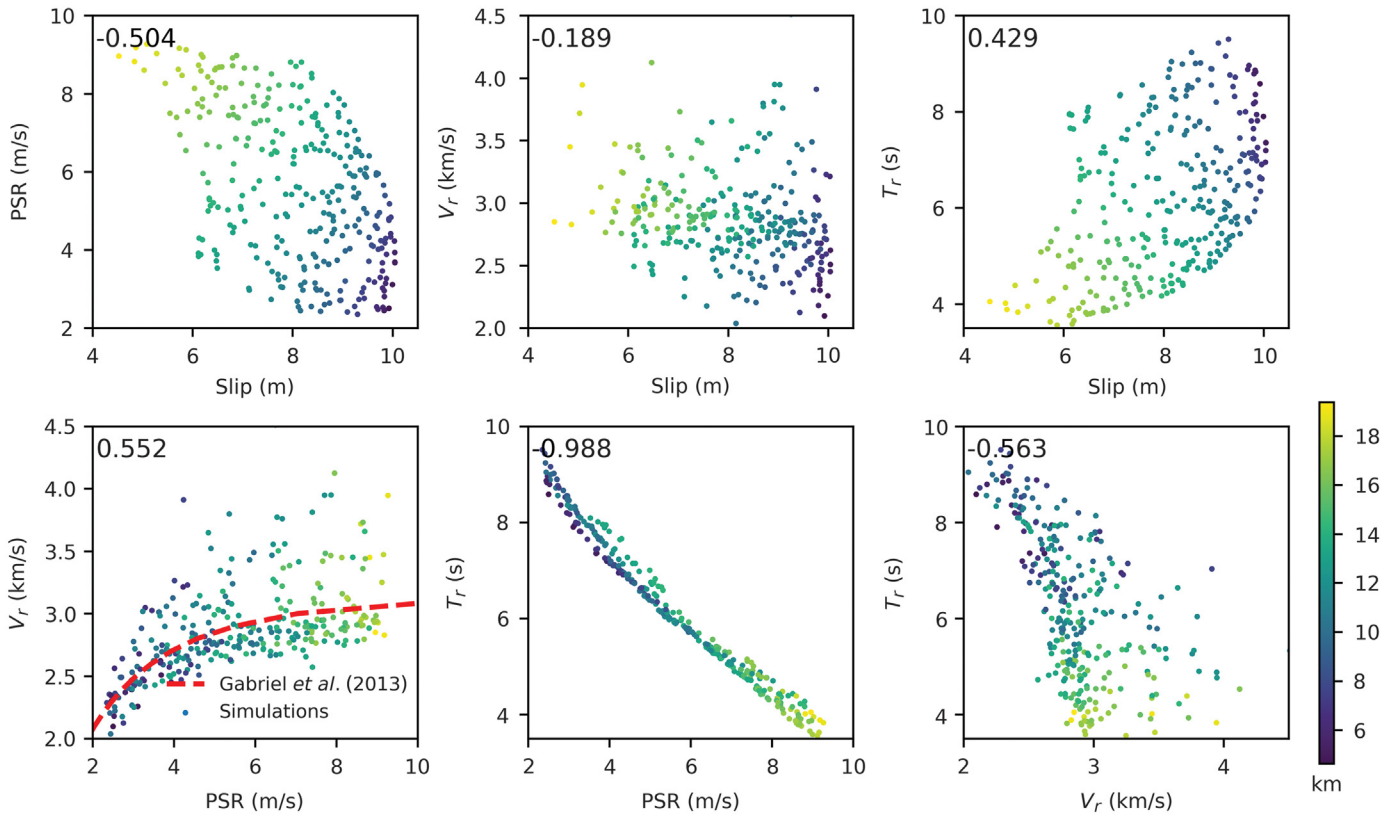

Figure 8. Correlations between rupture parameters, averaged over all 49 simulations, for six pairs of rupture variables and at all fault receivers. The correlation coefficient computed from the averaged dataset is shown in the top-left corner of each subplot. Dots are color coded by hypocenter–receiver distance. The bottom-left panel also shows the theoretical model of Gabriel *et al.* (2013) for comparison.

distance R_{JB} using the orientation-independent PGV metric GMRotD50 (Boore *et al.*, 2006). Figure 10 shows the distance dependence of the mean ($\mu_{\ln(PGV)}$) and standard deviation ($\phi_{\ln(PGV)}$) of ln(PGV) for varying α_{hy} and w. The mean PGV decreases more strongly with increasing w than with increasing α_{hy}: $\mu_{\ln(PGV)}$ decreases by nearly 15% at $R_{JB} = 80$ km if w is doubled, but by only 2% when α_{hy} is doubled. The variability $\phi_{\ln(PGV)}$ has a similar trend for all R_{JB} distances for both α_{hy} and w except at very short distances ($R_{JB} = 1$ km). We also observe increased ground-motion variability $\phi_{\ln(PGV)}$ beyond $R_{JB} = 15$ km, consistent with increased variability with distance for bilateral ruptures (Imtiaz *et al.*, 2015); because the rupture models in this study are predominantly bilateral, this effect cannot be attributed to TP alone. In summary, we observe that w strongly influences ground-motion velocity waveforms, in terms of arrival times and PGV values, whereas α_{hy} does not. Consequently, we postulate that advanced ground-motion simulations for seismic hazard purposes should consider accounting for the effects of shear-zone half-width w.

DISCUSSION AND CONCLUSIONS

Our simulations and subsequent analysis revealed that two key parameters of TP, hydraulic diffusivity α_{hy}, and shear-zone half-width w, have distinctly different effects on rupture behavior and the resulting near-source seismic wavefield. Let us not only summarize and place our key findings in context with the previous studies, but also speculate about further implications of our results.

We find that w has a stronger effect on rupture dynamics, kinematic rupture properties, and ground shaking than α_{hy}. Mean slip and rise time decrease with increasing α_{hy}, whereas mean PSR and rupture speed remain nearly constant. Mean slip, PSR, and rupture speed decreases with increasing w, whereas mean rise time increases. In addition, w distinctly affects the correlation between rupture parameters, especially between parameter pairs (slip, rupture speed), (PSR, rupture speed), (rupture speed, rise time), whereas α_{hy} has a negligible effect on rupture-parameter correlations. Mean PGV decreases faster with increasing w than with increasing α_{hy}, whereas ground-motion variability has similar trends.

The dominant impact of w compared to α_{hy} on rupture dynamics can be interpreted by considering the characteristic diffusion-process time t_{diff}, given as

$$t_{diff} \propto \frac{w^2}{\sqrt{\alpha_{th}^2 + \alpha_{hy}^2}}. \quad (16)$$

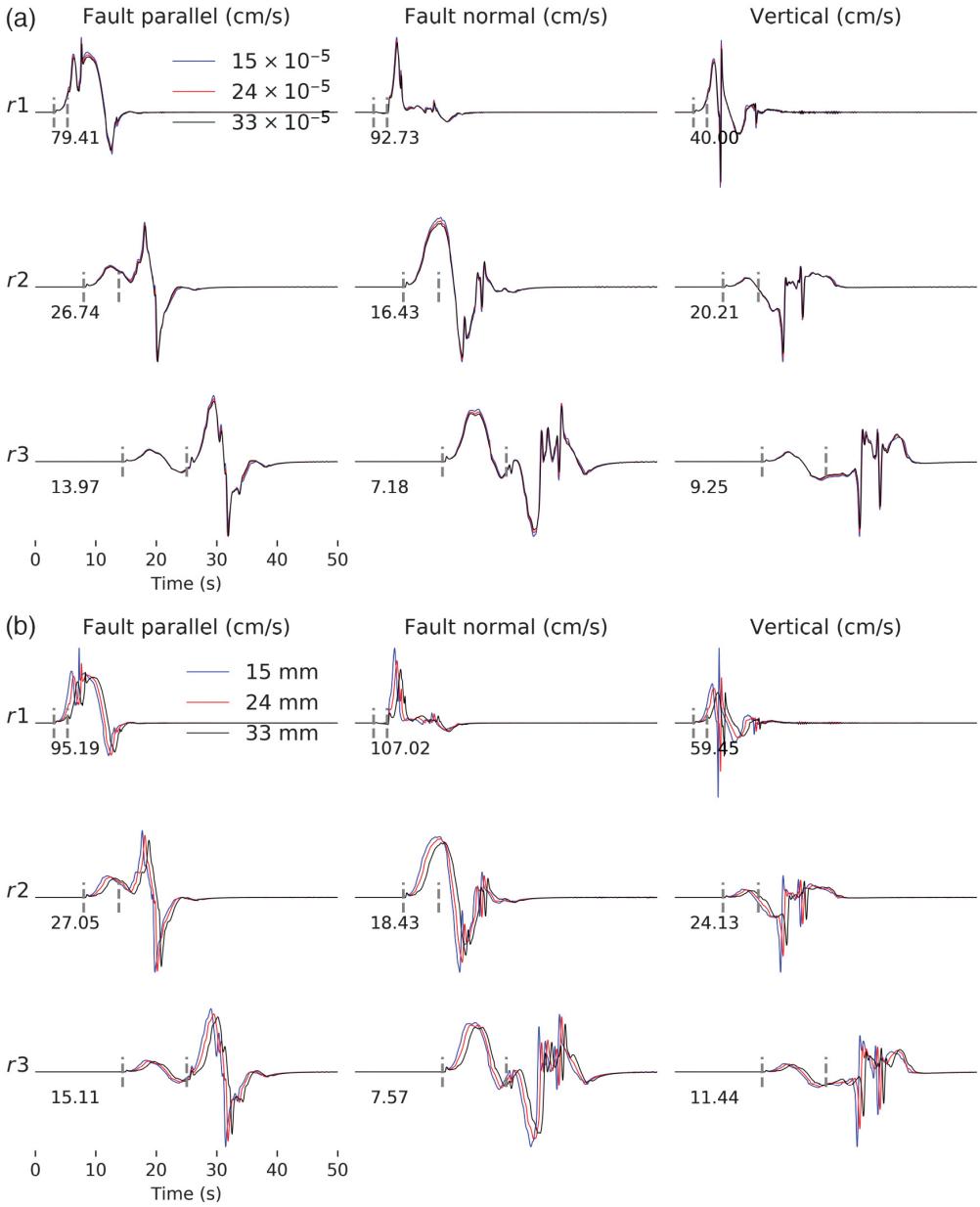

Figure 9. Comparison of ground velocity time histories (cm/s) at three receivers (*r*1–*r*3, Fig. 1b) for varying (a) hydraulic diffusivity α_{hy} and (b) shear-zone half-width w. Gray dashed bars show theoretical *P*- and *S*-wave arrival times from the hypocenter. Waveforms are normalized with respect to the peak absolute value (indicated in the bottom left) for each component.

Because $\alpha_{th} \ll \alpha_{hy}$,

$$t_{diff} \approx \frac{w^2}{\alpha_{hy}}. \quad (17)$$

From equation (17) we infer that t_{diff} increases by a factor 4 as w doubles, whereas it decreases only by a factor 2 as α_{hy} is doubled. This general behavior is illustrated in Figure 11 that shows variations in kinematic rupture parameters (slip, PSR, V_r, and T_r) as a function of $\frac{1}{\alpha_{hy}}$ and w^2, along with contours of diffusion time. The correlation between T_r and t_{diff} is most obvious, but trends in other rupture parameters emerge as well.

Large variations in diffusion time indicated by the vertical arrow in Figure 11 cause larger changes in mean slip, PSR, V_r, and T_r. Similarly, small variations in t_{diff} (horizontal arrow) lead to smaller alterations in source parameters. Hence, larger variations in t_{diff} for doubled w exert a strong influence on kinematic rupture properties and hence ground-motion patterns compared to doubling α_{hy}.

For 2D steady-state pulse-like ruptures under TP, Garagash (2012) developed analytical scaling relations. They show that rupture speed decreases with increasing principal shear zone thickness, consistent with our findings (Fig. 5). Their Figure 5a shows that pulse duration (i.e., rise time) scales with the characteristic diffusion time across the shear zone for a given value of prestress; that is, fault restrengthening due to pore pressure diffusion away from the shear zone becomes effective at this time scale. Increasing the rate of hydrothermal diffusion from the shear zone favors strength recovery, resulting in slip deceleration and eventually fault relocking (Garagash, 2012; Viesca and Garagash, 2015). This effect explains the relationship between rise time and diffusion time in Figure 11, and our findings of a strong influence of shear-zone half-width w and the weaker influence of hydraulic diffusivity α_{hy} on 3D heterogeneous rupture pulse characteristics. Our modeled rupture pulses have relatively long rise times (on the order of 5 s). Thus, healing will not only be governed by pore pressure diffusion as in the case of 2D steady-state pulses but also by geometrical effects such as the limited width of the seismogenic zone (Weng and Ampuero, 2019).

Mean slip decreases by almost 10% as α_{hy} or w increases by factor 2, reducing thereby the earthquake's moment magnitude by ~0.04 magnitude units. TP is efficient for small α_{hy} or w.

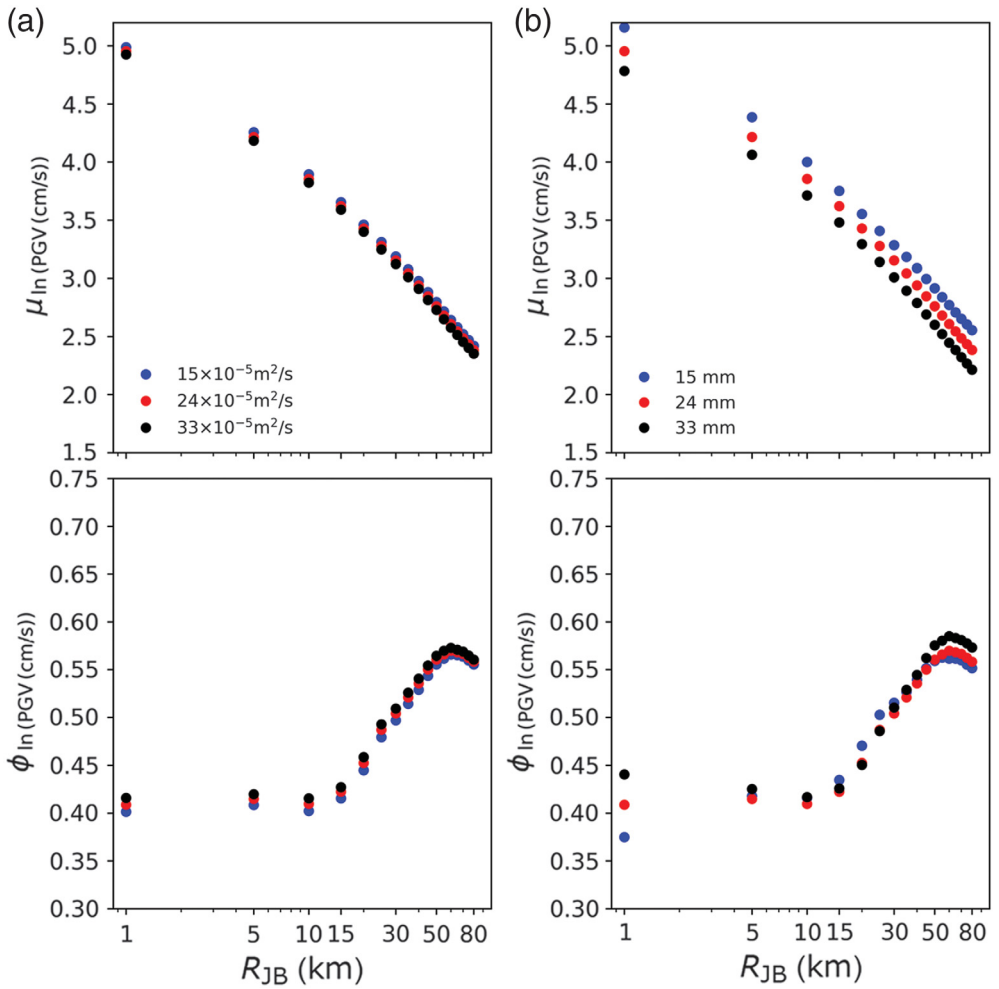

Figure 10. Distance dependence of mean $\mu_{ln(PGV)}$ and standard deviation $\phi_{ln(PGV)}$ of ln(PGV) for (a) varying hydraulic diffusivity α_{hy} and (b) shear-zone half-width w. Colors represent different α_{hy} and w-values.

Therefore, the magnitude of megathrust earthquakes occurring in fluid-rich subduction zone environments can be underestimated if TP effects are not considered in numerical modeling. We also observe a nearly 60% decrease in PSR as we double w, which is expected to affect ground-shaking amplitudes. Hence, future simulation studies for seismic hazard assessment from induced or megathrust events may consider accounting for TP effects.

Our simulations show almost no correlation between slip and rupture speed (Fig. 8). Past studies suggest a complex relationship between slip and V_r. Some dynamic rupture models show almost no correlation between these parameters (Schmedes *et al.*, 2010; Mai *et al.*, 2018), consistent with our findings, whereas others indicate that faster V_r correlates with areas of large slip (Oglesby and Day, 2002; Guatteri *et al.*, 2003). We also observe a slight increase in negative correlation, with r reducing from −0.1 to −0.3 between slip and V_r as w is doubled (Fig. 7). Therefore, the correlation of slip with V_r is nonunique and varies depending on TP parameter values, fault stress, and frictional conditions.

Pseudodynamic rupture generators calculate the spatial variation of T_r and V_r over the rupture plane assuming correlation with slip (e.g., Liu *et al.*, 2006; Graves and Pitarka, 2016). Our simulations suggest a lower (∼40%) correlation between slip and T_r than reported in earlier studies (∼50%–70%; e.g., Schmedes *et al.*, 2010; Mai *et al.*, 2018). However, these studies used linear slip-weakening friction and did not consider TP. Therefore, it may be to update rupture generators to account for TP effects, in particular, if they are applied to generate kinematic source models for ground-motion simulations in fluid-rich environments (such as in subduction zone settings).

Our study considers constant values for hydraulic diffusivity and shear-zone half-width over the main rupture plane (the velocity-weakening portion of the fault in Fig. 1a). However, in nature, spatial variations of TP are to be expected due to variations in rock properties, on-fault stress, and geometrical complexities. Studying the effects of spatially varying TP parameters is left for future work, in which one may also need to consider the potential correlations of TP parameters with geological and/or rupture-physics parameters. Regarding the effects of TP on ground-motion characteristics, we remark that we deliberately use a homogeneous half-space. We do not consider any path effects incurred by more complicated Earth structures such as layered 1D velocity structure, 3D Earth models, 3D small-scale heterogeneity, or viscoelastic attenuation, as our objective is to understand the first-order source effects due to TP. Future extensions of our study may include additional physical processes, that is, fault roughness, heterogeneous initial shear stress, plastic deformation of off-fault materials, increased fault-zone hydraulic diffusivity due to coseismic damage, to gain a deeper understanding of how TP may affect rupture dynamics under more realistic conditions. Correspondingly, 3D Earth structure and topography leading to seismic scattering that alters near-source (high frequency) ground-motion behavior may be additionally

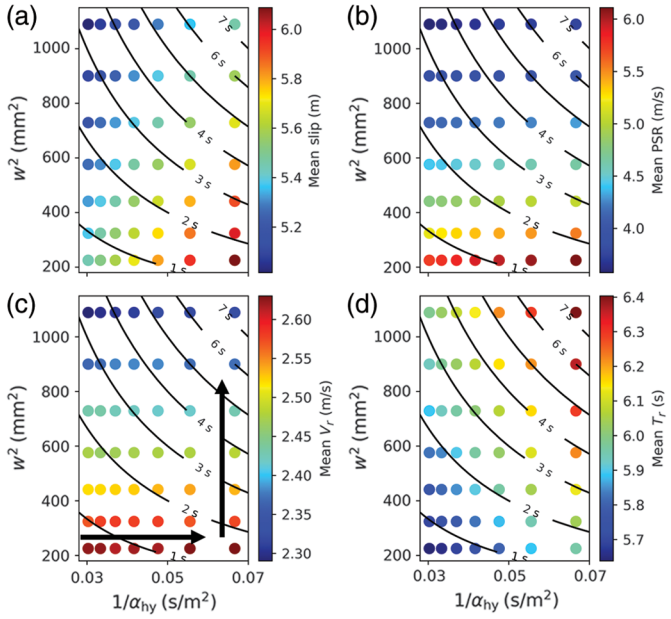

Figure 11. Variations of (a) mean slip, (b) PSR, (c) rupture speed, and (d) rise time as a function of $1/\alpha_{hy}$ and w^2. Contour lines mark diffusion time (equation 17). Horizontal and vertical black arrows mark directions of small and large variations in diffusion time, respectively.

considered (Imperatori and Mai, 2012; Shi and Day, 2013; Mai *et al.*, 2018; Vyas *et al.*, 2018, 2021; Wollherr *et al.*, 2018; Taufiqurrahman *et al.*, 2022). Modeling the combined effects of these physical processes may reduce (or enhance) TP effects on rupture dynamics and shaking levels, or may potentially render TP a second-order process.

In summary, our physics-based dynamic rupture simulations accounting for TP advance the understanding of the effects of hydraulic diffusivity and shear-zone half-width on rupture dynamics, kinematic source properties, and ground-motion characteristics. Our findings reveal how variations in α_{hy} and w determine slip, PSR, V_r, T_r, and their mutual correlation behavior; our results also show the effects of TP on near-source ground motions. Therefore, our findings provide important insights for earthquake source modelers and the seismic hazard community about rupture properties and ground-motion behavior for earthquakes in fluid-rich environments (georeservoirs or subduction zone settings).

DATA AND RESOURCES

We use the open-source software SeisSol (https://github.com/SeisSol/SeisSol, git commit hash: 2f4942e8de21aebd56e179eb11837acd40ae4c07) to simulate earthquake rupture dynamics and resulting ground-motion time series. SeisSol input files required to reproduce our simulations are available on zenodo repository (doi: 10.5281/zenodo.7789999). The almost 2.0 TB data generated in this work can be provided upon request to the authors. This article comprises an supplemental material on the temporal evolution of slip rate, total traction, temperature, and pressure at different on-fault locations, a description of the effects of hydraulic diffusivity, and shear-zone half-width variations on moment magnitude, and details of how to define the initial shear stress and rupture nucleation. The 3D benchmark exercise by Ulrich *et al.* (2020) is available on the Southern California Earthquake Center (SCEC) website (https://strike.scec.org/cvws/download/TPV105-3D-description.pdf). All websites were last accessed in October 2022.

DECLARATION OF COMPETING INTERESTS

The authors acknowledge that there are no conflicts of interest recorded.

ACKNOWLEDGMENTS

The authors acknowledge the work of and helpful discussions with Stephanie Wollherr, Sebastian Anger, and Kadek Palgunadi on the thermal pressurization (TP) implementation in SeisSol. The authors also thank Michael Barall and Yongfei Wang for uploading their solutions to the TPV105-3D benchmark exercise to the Southern California Earthquake Center (SCEC) platform. The research presented in this article is supported by the King Abdullah University of Science and Technology (KAUST) in Thuwal, Saudi Arabia, under Grant Numbers BAS/1/1339-01-01 and URF/1/3389-01-01 (Jagdish Chandra Vyas and Paul Martin Mai). Alice-Agnes Gabriel and Thomas Ulrich acknowledge the support of the European Research Council (ERC) under the European Union's Horizon 2020 research and innovation program (ERC Starting Grant TEAR, Grant Agreement Number 852992), Horizon Europe (ChEESE-2P Grant Number 101093038, DT-GEO Grant Number 101058129, and Geo-INQUIRE Grant Number 101058518), the SCEC (Grant Number 22135), the National Science Foundation (NSF, Grant Number EAR-2121666), the National Aeronautics and Space Administration (NASA, Grant Number 80NSSC20K0495), and the Bavarian State Ministry for Science and Art in the framework of the project Geothermal-Alliance Bavaria. Jean-Paul Ampeuro acknowledges the support of the French government through the Investments in the Future project UCAJEDI (ANR-15-IDEX-01) managed by the French National Research Agency (ANR). Earthquake rupture dynamics and ground-motion modeling have been carried out using the KAUST Supercomputing Laboratory (KSL), and the authors acknowledge the support of the KSL staff. The authors also thank Kadek Palgunadi and the SeisSol software team (https://seissol.org/, last accessed April 2023) for their support during the software installation.

REFERENCES

Abercrombie, R. E., and J. R. Rice (2005). Can observations of earthquake scaling constrain slip weakening? *Geophys. J. Int.* **162,** no. 2, 406–424.

Acosta, M., F. Passelègue, A. Schubnel, and M. Violay (2018). Dynamic weakening during earthquakes controlled by fluid thermodynamics, *Nat. Commun.* **9,** no. 1, 1–9.

Ampuero, J.-P., and A. M. Rubin (2008). Earthquake nucleation on rate and state faults–Aging and slip laws, *J. Geophys. Res.* **113,** no. B1, doi: 10.1029/2007JB005082.

Andrews, D. (2005). Thermal pressurization explains enhanced long-period motion in the Chi-Chi earthquake, *AGU Fall Meeting Abstracts*, Vol. 2005, S34A–04.

Andrews, D. J. (2002). A fault constitutive relation accounting for thermal pressurization of pore fluid, *J. Geophys. Res.* **107,** no. B12, ESE 15-1–ESE 15-8.

Aretusini, S., F. Meneghini, E. Spagnuolo, C. Harbord, and G. Di Toro (2021). Fluid pressurisation and earthquake propagation in the Hikurangi subduction zone, *Nat. Commun.* **12,** no. 1, 1–8.

Badt, N. Z., T. E. Tullis, G. Hirth, and D. L. Goldsby (2020). Thermal pressurization weakening in laboratory experiments, *J. Geophys. Res.* **125,** no. 5, e2019JB018872, doi: 10.1029/2019JB018872.

Beeler, N., T. Tullis, and D. Goldsby (2008). Constitutive relationships and physical basis of fault strength due to flash heating, *J. Geophys. Res.* **113,** no. B1, doi: 10.1029/2007JB004988.

Bizzarri, A., and M. Cocco (2006a). A thermal pressurization model for the spontaneous dynamic rupture propagation on a three-dimensional fault: 1. methodological approach, *J. Geophys. Res.* **111,** no. B5, doi: 10.1029/2005JB003862.

Bizzarri, A., and M. Cocco (2006b). A thermal pressurization model for the spontaneous dynamic rupture propagation on a three-dimensional fault: 2. traction evolution and dynamic parameters, *J. Geophys. Res.* **111,** no. B5, doi: 10.1029/2005JB003862.

Boore, D. M., J. Watson-Lamprey, and N. A. Abrahamson (2006). Orientation-independent measures of ground motion, *Bull. Seismol. Soc. Am.* **96,** no. 4A, 1502–1511.

Brantut, N., D. I. Garagash, and H. Noda (2019). Stability of pulse-like earthquake ruptures, *J. Geophys. Res.* **124,** no. 8, 8998–9020.

Cocco, M., P. Spudich, and E. Tinti (2006). On the mechanical work absorbed on faults during earthquake ruptures, in *Radiated Energy and the Physics of Earthquakes Faulting*, R. Abercrombie, A. McGarr, H. Kanamori, and G. Di Toro (Editors), AGU, available at http://hdl.handle.net/2122/2290 (last accessed April 2023).

Crempien, J. G., and R. J. Archuleta (2018). Within-event and between-events ground motion variability from earthquake rupture scenarios, in *Best Practices in Physics-based Fault Rupture Models for Seismic Hazard Assessment of Nuclear Installations*, L. A. Dalguer, Y. Fukushima, K. Irikura, and C. Wu (Editors), Springer, Cham, Switzerland, 127–141.

Di Toro, G., D. L. Goldsby, and T. E. Tullis (2004). Friction falls towards zero in quartz rock as slip velocity approaches seismic rates, *Nature* **427,** no. 6973, 436–439.

Di Toro, G., R. Han, T. Hirose, N. De Paola, S. Nielsen, K. Mizoguchi, F. Ferri, M. Cocco, and T. Shimamoto (2011). Fault lubrication during earthquakes, *Nature* **471,** no. 7339, 494–498.

Dieterich, J. H. (1972). Time-dependent friction in rocks, *J. Geophys. Res.* **77,** no. 20, 3690–3697.

Dieterich, J. H. (1978). Time-dependent friction and the mechanics of stick-slip, in *Rock Friction and Earthquake Prediction*, J. D. Byerlee and M. Wyss (Editors), Birkhäuser, Basel, Switzerland, 790–806, doi: 10.1007/978-3-0348-7182-2.

Dieterich, J. H. (1981). Constitutive properties of faults with simulated gouge, in *Mechanical Behavior of Crustal Rocks: The Handin*, N. L. Carter, M. Friedman, J. M. Logan, and D. W. Stearns (Editors), Vol. 24, 103–120, doi: 10.1029/GM024.

Dieterich, J. H., and B. Kilgore (1996). Implications of fault constitutive properties for earthquake prediction, *Proc. Natl. Acad. Sci. Unit. States Am.* **93,** no. 9, 3787–3794.

Dumbser, M., and M. Käser (2006). An arbitrary high-order discontinuous Galerkin method for elastic waves on unstructured meshes—II. The three-dimensional isotropic case, *Geophys. J. Int.* **167,** no. 1, 319–336.

Dunham, E. M., D. Belanger, L. Cong, and J. E. Kozdon (2011). Earthquake ruptures with strongly rate-weakening friction and off-fault plasticity, part 1: Planar faults, *Bull. Seismol. Soc. Am.* **101,** no. 5, 2296–2307.

Gabriel, A., J. Vyas, T. Ulrich, J. Ampuero, and M. Mai (2020). 3d dynamic rupture modeling with thermal pressurization, *Poster Presentation at 2020 SCEC Annual Meeting*, Southern California Earthquake Center, 158 pp.

Gabriel, A.-A., J.-P. Ampuero, L. Dalguer, and P. M. Mai (2013). Source properties of dynamic rupture pulses with off-fault plasticity, *J. Geophys. Res.* **118,** no. 8, 4117–4126.

Galis, M., J. P. Ampuero, P. M. Mai, and F. Cappa (2017). Induced seismicity provides insight into why earthquake ruptures stop, *Sci. Adv.* **3,** no. 12, eaap7528, doi: 10.1126/sciadv.aap7528.

Galis, M., J.-P. Ampuero, P. M. Mai, and J. Kristek (2019). Initiation and arrest of earthquake ruptures due to elongated overstressed regions, *Geophys. J. Int.* **217,** no. 3, 1783–1797.

Gallovič, F. (2017). Azimuthal dependence of the ground motion variability from scenario modeling of the 2014 Mw 6.0 South Napa, California, earthquake using an advanced kinematic source model, *Pure Appl. Geophys.* **174,** no. 9, 3467–3478.

Garagash, D. (2012). Seismic and aseismic slip pulses driven by thermal pressurization of pore fluid, *J. Geophys. Res.* **117,** no. B4, doi: 10.1029/2011JB008889.

Graves, R., and A. Pitarka (2016). Kinematic ground-motion simulations on rough faults including effects of 3d stochastic velocity perturbations, *Bull. Seismol. Soc. Am.* **106,** no. 5, 2136–2153.

Grzemba, B. (2015). New experimental investigations on the Dieterich-Ruina friction law, *FU Mech. Eng.* **13,** no. 1, 11–20.

Gu, J. (1984). Frictional resistance to accelerating slip, *Pure Appl. Geophys.* **122,** 662–679.

Gu, J. (1986). Friction constitutive law with rate and state dependences, *Pure Appl. Geophys.* **124,** 773–791.

Gu, J.-C., J. R. Rice, A. L. Ruina, and T. T. Simon (1984). Slip motion and stability of a single degree of freedom elastic system with rate and state dependent friction, *J. Mech. Phys. Solids* **32,** no. 3, 167–196.

Guatteri, M., P. M. Mai, G. C. Beroza, and J. Boatwright (2003). Strong ground-motion prediction from stochastic-dynamic source models, *Bull. Seismol. Soc. Am.* **93,** no. 1, 301–313.

Harris, R. A., M. Barall, B. Aagaard, S. Ma, D. Roten, K. Olsen, B. Duan, D. Liu, B. Luo, K. Bai, *et al.* (2018). A suite of exercises for verifying dynamic earthquake rupture codes, *Seismol. Res. Lett.* **89,** no. 3, 1146–1162.

Harris, R. A., M. Barall, D. J. Andrews, B. Duan, S. Ma, E. M. Dunham, A.-A. Gabriel, Y. Kaneko, Y. Kase, B. T. Aagaard, *et al.* (2011). Verifying a computational method for predicting extreme ground motion, *Seismol. Res. Lett.* **82,** no. 5, 638–644.

Hirono, T., K. Tsuda, W. Tanikawa, J.-P. Ampuero, B. Shibazaki, M. Kinoshita, and J. J. Mori (2016). Near-trench slip potential of megaquakes evaluated from fault properties and conditions, *Sci. Rep.* **6,** no. 1, 1–13.

Imperatori, W., and P. M. Mai (2012). Sensitivity of broad-band ground-motion simulations to earthquake source and earth structure variations: An application to the Messina straits (Italy), *Geophys. J. Int.* **188,** no. 3, 1103–1116.

Imtiaz, A., M. Causse, E. Chaljub, and F. Cotton (2015). Is ground-motion variability distance dependent? Insight from finite-source rupture simulations, *Bull. Seismol. Soc. Am.* **105,** no. 2A, 950–962.

Kaneko, Y., N. Lapusta, and J.-P. Ampuero (2008). Spectral element modeling of spontaneous earthquake rupture on rate and state faults: Effect of velocity-strengthening friction at shallow depths, *J. Geophys. Res.* **113,** no. B9, doi: 10.1029/2007JB005553.

Kranz, R., J. Saltzman, and J. Blacic (1990). Hydraulic diffusivity measurements on laboratory rock samples using an oscillating pore pressure method, *Int. J. Rock Mech. Min. Sci. Geomech. Abstr.* **27,** 345–352.

Lachenbruch, A. H. (1980). Frictional heating, fluid pressure, and the resistance to fault motion, *J. Geophys. Res.* **85,** no. B11, 6097–6112.

Lachenbruch, A. H., and J. Sass (1980). Heat flow and energetics of the San Andreas Fault zone, *J. Geophys. Res.* **85,** no. B11, 6185–6222.

Lamb, S. (2006). Shear stresses on megathrusts: Implications for mountain building behind subduction zones, *J. Geophys. Res.* **111,** no. B7, doi: 10.1029/2005JB003916.

Lambert, V., N. Lapusta, and S. Perry (2021). Propagation of large earthquakes as self-healing pulses or mild cracks, *Nature* **591,** no. 7849, 252–258.

Li, J.-R., and L. Greengard (2007). On the numerical solution of the heat equation i: Fast solvers in free space, *J. Comput. Phys.* **226,** no. 2, 1891–1901.

Liu, P., R. J. Archuleta, and S. H. Hartzell (2006). Prediction of broadband ground-motion time histories: Hybrid low/high-frequency method with correlated random source parameters, *Bull. Seismol. Soc. Am.* **96,** no. 6, 2118–2130.

Madden, E. H., T. Ulrich, and A.-A. Gabriel (2022). The state of pore fluid pressure and 3-D megathrust earthquake dynamics, *J. Geophys. Res.* **127,** no. 4, e2021JB023382, doi: 10.1029/2021JB023382.

Mai, P. M., M. Galis, K. K. Thingbaijam, J. C. Vyas, and E. M. Dunham (2018). Accounting for fault roughness in pseudo-dynamic ground-motion simulations, in *Best Practices in Physics-based Fault Rupture Models for Seismic Hazard Assessment of Nuclear Installations*, L. A. Dalguer, Y. Fukushima, K. Irikura, and C. Wu (Editors), Springer, 95–126, doi: 10.1007/978-3-319-72709-7_7.

Marone, C., and C. Scholz (1988). The depth of seismic faulting and the upper transition from stable to unstable slip regimes, *Geophys. Res. Lett.* **15,** no. 6, 621–624.

Mase, C. W., and L. Smith (1984). Pore-fluid pressures and frictional heating on a fault surface, *Pure Appl. Geophys.* **122,** no. 2, 583–607.

Mase, C. W., and L. Smith (1987). Effects of frictional heating on the thermal, hydrologic, and mechanical response of a fault, *J. Geophys. Res.* **92,** no. B7, 6249–6272.

Mena, B., L. Dalguer, and P. M. Mai (2012). Pseudodynamic source characterization for strike-slip faulting including stress heterogeneity and super-shear ruptures, *Bull. Seismol. Soc. Am.* **102,** no. 4, 1654–1680.

Mitsui, Y., and M. Cocco (2010). The role of porosity evolution and fluid flow in frictional instabilities: A parametric study using a spring-slider dynamic system, *Geophys. Res. Lett.* **37,** no. 23, doi: 10.1029/2010GL045672.

Mitsui, Y., Y. Iio, and Y. Fukahata (2012). A scenario for the generation process of the 2011 Tohoku earthquake based on dynamic rupture simulation: Role of stress concentration and thermal fluid pressurization, *Earth Planets Space* **64,** no. 12, 1177–1187.

Noda, H., E. M. Dunham, and J. R. Rice (2009). Earthquake ruptures with thermal weakening and the operation of major faults at low overall stress levels, *J. Geophys. Res.* **114,** no. B7, doi: 10.1029/2008JB006143.

Noda, H., and N. Lapusta (2010). Three-dimensional earthquake sequence simulations with evolving temperature and pore pressure due to shear heating: Effect of heterogeneous hydraulic diffusivity, *J. Geophys. Res.* **115,** no. B12, doi: 10.1029/2010JB007780.

Noda, H., and N. Lapusta (2013). Stable creeping fault segments can become destructive as a result of dynamic weakening, *Nature* **493,** no. 7433, 518–521.

Oglesby, D. D., and S. M. Day (2002). Stochastic fault stress: Implications for fault dynamics and ground motion, *Bull. Seismol. Soc. Am.* **92,** no. 8, 3006–3021.

Pelties, C., A.-A. Gabriel, and J.-P. Ampuero (2014). Verification of an ADER-DG method for complex dynamic rupture problems, *Geosci. Model Dev.* **7,** no. 3, 847–866.

Perry, S. M., V. Lambert, and N. Lapusta (2020). Nearly magnitude-invariant stress drops in simulated crack-like earthquake sequences on rate-and-state faults with thermal pressurization of pore fluids, *J. Geophys. Res.* **125,** no. 3, e2019JB018597, doi: 10.1029/2019JB018597.

Rabinowicz, E. (1958). The intrinsic variables affecting the stick-slip process, *Proc. Phys. Soc.* **71,** no. 4, 668.

Rabinowicz, E. (1959). A study of the stick-slip process, in *Friction and Wear*, R. Davies (Editor), Elsevier, New York.

Rice, J. R. (2006). Heating and weakening of faults during earthquake slip, *J. Geophys. Res.* **111,** no. B5, doi: 10.1029/2005JB004006.

Rodriguez-Marek, A., G. A. Montalva, F. Cotton, and F. Bonilla (2011). Analysis of single-station standard deviation using the KiK-net data, *Bull. Seismol. Soc. Am.* **101,** no. 3, 1242–1258.

Ruina, A. (1980). Friction laws and instabilities: A quasi-static analysis of some dry friction behavior, *Ph.D. Thesis*, Division of Engineering, Brown University.

Ruina, A. (1983). Slip instability and state variable friction laws, *J. Geophys. Res.* **88,** no. B12, 10,359–10,370.

Schmedes, J., R. J. Archuleta, and D. Lavallée (2010). Correlation of earthquake source parameters inferred from dynamic rupture simulations, *J. Geophys. Res.* **115,** no. B3, doi: 10.1029/2009JB006689.

Schmedes, J., R. J. Archuleta, and D. Lavallée (2013). A kinematic rupture model generator incorporating spatial interdependency of earthquake source parameters, *Geophys. J. Int.* **192,** no. 3, 1116–1131.

Schmitt, S. V., P. Segall, and E. M. Dunham (2015). Nucleation and dynamic rupture on weakly stressed faults sustained by thermal pressurization, *J. Geophys. Res.* **120,** no. 11, 7606–7640.

Scholz, C. H. (1998). Earthquakes and friction laws, *Nature* **391,** no. 6662, 37–42.

Scholz, C. H. (2019). *The Mechanics of Earthquakes and Faulting*, Cambridge University Press, Cambridge, United Kingdom.

Shi, Z., and S. M. Day (2013). Rupture dynamics and ground motion from 3-d rough-fault simulations, *J. Geophys. Res.* **118,** no. 3, 122–1141.

Sibson, R. (1973). Interactions between temperature and pore-fluid pressure during earthquake faulting and a mechanism for partial or total stress relief, *Nat. Phys. Sci.* **243,** no. 126, 66–68.

Sibson, R. (1980). Power dissipation and stress levels on faults in the upper crust, *J. Geophys. Res.* **85,** no. B11, 6239–6247.

Sibson, R. H. (1977). Kinetic shear resistance, fluid pressures and radiation efficiency during seismic faulting, *Pure Appl. Geophys.* **115,** no. 1, 387–400.

Song, S. G., L. A. Dalguer, and P. M. Mai (2014). Pseudo-dynamic source modelling with 1-point and 2-point statistics of earthquake source parameters, *Geophys. J. Int.* **196,** no. 3, 1770–1786.

Spagnuolo, E., S. Nielsen, M. Violay, and G. Di Toro (2016). An empirically based steady state friction law and implications for fault stability, *Geophys. Res. Lett.* **43,** no. 7, 3263–3271.

Suzuki, T., and T. Yamashita (2006). Nonlinear thermoporoelastic effects on dynamic earthquake rupture, *J. Geophys. Res.* **111,** no. B3, doi: 10.1029/2005JB003810.

Taufiqurrahman, T., A.-A. Gabriel, T. Ulrich, L. Valentová, and F. Gallovič (2022). Broadband dynamic rupture modeling with fractal fault roughness, frictional heterogeneity, viscoelasticity and topography: The 2016 Mw 6.2 Amatrice, Italy earthquake, *Geophys. Res. Lett.* **49,** no. 22, e2022GL098872, doi: 10.1029/2022GL098872.

Tinti, E., P. Spudich, and M. Cocco (2005). Earthquake fracture energy inferred from kinematic rupture models on extended faults. *J. Geophys. Res.* **110,** no. B12, doi: 10.1029/2005JB003644.

Ujiie, K., M. Kameyama, and A. Yamaguchi (2010). Geological record of thermal pressurization and earthquake instability of subduction thrusts, *Tectonophysics* **485,** nos. 1/4, 260–268.

Ulrich, T., J. Vyas, and A. Gabriel (2020). SCEC code verification: A proposed 3d benchmark of thermal pressurization and rate-and-state strong velocity weakening friction, *SCEC/USGS Benchmark Descriptions: TPV105-3D*, The SCEC/USGS Spontaneous Rupture Code Verification Project.

Uphoff, C., S. Rettenberger, M. Bader, E. H. Madden, T. Ulrich, S. Wollherr, and A.-A. Gabriel (2017). Extreme scale multi-physics simulations of the tsunamigenic 2004 Sumatra megathrust earthquake, *Proc. of the International Conf. for High Performance Computing, Networking, Storage and Analysis*, 1–16.

Urata, Y., S. Hok, E. Fukuyama, and R. Madariaga (2014). The effect of thermal pressurization on dynamic fault branching, *Geophys. J. Int.* **196,** no. 2, 1237–1246.

Verberne, B. A., O. Plümper, and C. J. Spiers (2019). Nanocrystalline principal slip zones and their role in controlling crustal fault rheology, *Minerals* **9,** no. 6, 328.

Viesca, R. C., and D. I. Garagash (2015). Ubiquitous weakening of faults due to thermal pressurization, *Nature Geosci.* **8,** no. 11, 875–879.

Vyas, J. C., M. Galis, and P. M. Mai (2021). Characterizing seismic scattering in 3d heterogeneous earth by a single parameter, *Bull. Seismol. Soc. Am.* **111,** no. 2, 791–800.

Vyas, J. C., P. M. Mai, and M. Galis (2016). Distance and azimuthal dependence of ground-motion variability for unilateral strike-slip ruptures, *Bull. Seismol. Soc. Am.* **106,** no. 4, 1584–1599.

Vyas, J. C., P. M. Mai, M. Galis, E. M. Dunham, and W. Imperatori (2018). Mach wave properties in the presence of source and medium heterogeneity, *Geophys. J. Int.* **214,** no. 3, 2035–2052.

Weng, H., and J.-P. Ampuero (2019). The dynamics of elongated earthquake ruptures, *J. Geophys. Res.* **124,** no. 8, 8584–8610.

Wibberley, C. A. (2002). Hydraulic diffusivity of fault gouge zones and implications for thermal pressurization during seismic slip, *Earth Planets Space* **54,** no. 11, 1153–1171.

Wibberley, C. A., and T. Shimamoto (2005). Earthquake slip weakening and asperities explained by thermal pressurization, *Nature* **436,** no. 7051, 689–692.

Wollherr, S., A.-A. Gabriel, and C. Uphoff (2018). Off-fault plasticity in three-dimensional dynamic rupture simulations using a modal discontinuous Galerkin method on unstructured meshes: Implementation, verification and application, *Geophys. J. Int.* **214,** no. 3, 1556–1584.

Youngs, R., N. Abrahamson, F. Makdisi, and K. Sadigh (1995). Magnitude-dependent variance of peak ground acceleration, *Bull. Seismol. Soc. Am.* **85,** no. 4, 1161–1176.

Zheng, G., and J. R. Rice (1998). Conditions under which velocity-weakening friction allows a self-healing versus a cracklike mode of rupture, *Bull. Seismol. Soc. Am.* **88,** no. 6, 1466–1483.

Zhu, W., K. L. Allison, E. M. Dunham, and Y. Yang (2020). Fault valving and pore pressure evolution in simulations of earthquake sequences and aseismic slip, *Nat. Commun.* **11,** no. 1, 4833.

Manuscript received 12 October 2022
Published online 10 May 2023